

See discussions, stats, and author profiles for this publication at: <https://www.researchgate.net/publication/45278576>

# Cenozoic Tectonics of Western North America Controlled by Evolving Width of Farallon Slab

Article in Science · July 2010

DOI: 10.1126/science.1190366 · Source: PubMed

CITATIONS

52

READS

477

5 authors, including:



**Wouter P. Schellart**

Vrije Universiteit Amsterdam (Netherlands)

131 PUBLICATIONS 3,663 CITATIONS

[SEE PROFILE](#)



**Dave R Stegman**

University of California, San Diego

59 PUBLICATIONS 1,994 CITATIONS

[SEE PROFILE](#)



**Rebecca Farrington**

University of Melbourne

16 PUBLICATIONS 314 CITATIONS

[SEE PROFILE](#)



**Louis Moresi**

Australian National University

300 PUBLICATIONS 7,647 CITATIONS

[SEE PROFILE](#)

Some of the authors of this publication are also working on these related projects:



BASIN GENESIS HUB – GEODYNAMICS AND EVOLUTION OF SEDIMENTARY SYSTEMS [View project](#)



Computational Geophysics [View project](#)

*This copy is for your personal, non-commercial use only.*

**If you wish to distribute this article to others**, you can order high-quality copies for your colleagues, clients, or customers by [clicking here](#).

**Permission to republish or repurpose articles or portions of articles** can be obtained by following the guidelines [here](#).

***The following resources related to this article are available online at [www.sciencemag.org](http://www.sciencemag.org) (this information is current as of September 12, 2010 ):***

**Updated information and services**, including high-resolution figures, can be found in the online version of this article at:

<http://www.sciencemag.org/cgi/content/full/329/5989/316>

**Supporting Online Material** can be found at:

<http://www.sciencemag.org/cgi/content/full/329/5989/316/DC1>

This article **cites 28 articles**, 7 of which can be accessed for free:

<http://www.sciencemag.org/cgi/content/full/329/5989/316#otherarticles>

This article appears in the following **subject collections**:

Geochemistry, Geophysics

[http://www.sciencemag.org/cgi/collection/geochem\\_phys](http://www.sciencemag.org/cgi/collection/geochem_phys)

Overall, reducing the wire diameter and increasing the lateral length of the wire can also effectively benefit the lowering of such stresses.

The growth rate of an electrodeposited wire is intrinsically limited by the rate of electroreduction, or more specifically by the diffusion-limited ionic current (22) described by a recessed microelectrode (the growth front of the deposited metal wire) in a truncated cone (the tapered dispensing end of the micropipette). Nonetheless, the growth rate might be increased through an increase in electrolyte concentration and/or the use of a short tapered micropipette. Alternatively, an array of micropipettes can be deployed to increase the wire-bonding throughput.

With the proper mechanical design and system control, this meniscus-confined 3D electrodeposition method can be used to fabricate more intricate microscale and nanoscale structures than those described here. Such structures could include designed structural and device functionalities integrating a variety of metallic materials, such as magnetic and noble metals and even metal alloys. Moreover, because it is intrinsically a low-cost direct-writing technology, this technique can be used to fabricate such micro- or nanostructures

on existing micro- or nanostructures when such fabrication becomes difficult or expensive with the traditional lithography process (fig. S3).

#### References and Notes

1. P. Ramm, J. M. Wolf, B. Wunderle, in *3-D IC Integration: Technology and Applications*, P. E. Garrou, P. Ramm, C. A. Bower, Eds. (Wiley-VCH, New York, 2008), pp. 289–318.
2. G. Harman, *Wire Bonding in Microelectronics* (McGraw-Hill, New York, 2009).
3. C. Harper, *Electronic Packaging and Interconnection Handbook* (McGraw-Hill, New York, 2005).
4. International Technology Roadmap for Semiconductors (ITRS-2007) ([www.itrs.net/Links/2007ITRS/Home2007.htm](http://www.itrs.net/Links/2007ITRS/Home2007.htm)).
5. T. Morita et al., *J. Vac. Sci. Technol. B* **21**, 2737 (2003).
6. B. Y. Ahn et al., *Science* **323**, 1590 (2009); published online 12 February 2009 (10.1126/science.1168375).
7. Y. Li, B. W. Maynor, J. Liu, *J. Am. Chem. Soc.* **123**, 2105 (2001).
8. J. D. Madden, I. W. Hunter, *J. Microelectromech. Syst.* **5**, 24 (1996).
9. J. Jang, G. C. Schatz, M. A. Ratner, *Phys. Rev. Lett.* **92**, 085504 (2004).
10. J. Jang, G. C. Schatz, M. A. Ratner, *Phys. Rev. Lett.* **90**, 156104 (2003).
11. R. C. Major, J. E. Houston, M. J. McGrath, J. I. Siepmann, X.-Y. Zhu, *Phys. Rev. Lett.* **96**, 177803 (2006).
12. A. P. Suryavanshi, M.-F. Yu, *Appl. Phys. Lett.* **88**, 083103 (2006).
13. A. P. Suryavanshi, M.-F. Yu, *Nanotechnology* **18**, 105305 (2007).
14. See supporting material on Science Online.
15. M. E. Toimil Molares et al., *Appl. Phys. Lett.* **82**, 2139 (2003).
16. Q. Huang, C. M. Lilley, M. Bode, R. Divan, *J. Appl. Phys.* **104**, 023709 (2008).
17. Q. Huang, C. M. Lilley, R. Divan, *Nanotechnology* **20**, 075706 (2009).
18. S. Karim, K. Maaz, G. Ali, W. Ensinger, *J. Phys. D* **42**, 185403 (2009).
19. R. Defay, I. Prigogine, *Surface Tension and Adsorption* (Longman, London, 1966).
20. H. Ghasemi, C. A. Ward, *J. Phys. Chem. C* **114**, 5088 (2010).
21. Y. A. Tatarchenko, *Shaped Crystal Growth* (Kluwer Academic, New York, 1993).
22. Y. H. Lanyon et al., *Anal. Chem.* **79**, 3048 (2007).
23. Supported by the Grainger Foundation. We acknowledge the use of microscopy facilities in the Center for Microanalysis of Materials at the University of Illinois at Urbana-Champaign. A U.S. patent application based on this work was filed by the University of Illinois on 7 June 2010.

#### Supporting Online Material

[www.sciencemag.org/cgi/content/full/329/5989/313/DC1](http://www.sciencemag.org/cgi/content/full/329/5989/313/DC1)  
Materials and Methods  
Figs. S1 to S3

5 April 2010; accepted 10 June 2010  
10.1126/science.1190496

## Cenozoic Tectonics of Western North America Controlled by Evolving Width of Farallon Slab

W. P. Schellart,<sup>1,\*</sup> D. R. Stegman,<sup>2,3</sup> R. J. Farrington,<sup>4</sup> J. Freeman,<sup>4,5</sup> L. Moresi<sup>1,4</sup>

Subduction of oceanic lithosphere occurs through two modes: subducting plate motion and trench migration. Using a global subduction zone data set and three-dimensional numerical subduction models, we show that slab width ( $W$ ) controls these modes and the partitioning of subduction between them. Subducting plate velocity scales with  $W^{2/3}$ , whereas trench velocity scales with  $1/W$ . These findings explain the Cenozoic slowdown of the Farallon plate and the decrease in subduction partitioning by its decreasing slab width. The change from Sevier-Laramide orogenesis to Basin and Range extension in North America is also explained by slab width; shortening occurred during wide-slab subduction and overriding-plate-driven trench retreat, whereas extension occurred during intermediate to narrow-slab subduction and slab-driven trench retreat.

Understanding the partitioning of plate consumption at subduction zones is vital for constraining its effect on mantle anisotropy, dynamic topography, and overriding plate deformation at subduction zones (1–3). Subduction partitioning also exerts an important control on slab geometry (4, 5) and the style of mantle stirring [i.e., poloidal versus toroidal flow (5–8)], providing

constraints on the geochemical heterogeneity of the mantle. It remains unclear, however, how the rate of plate consumption at oceanic trenches [the subduction velocity ( $v_{S,L}$ )] is partitioned into its two primary components, the trench-normal subducting plate velocity ( $v_{SP,L}$ ) and trench velocity ( $v_{TL}$ ), and what controls such partitioning. At present, variation in subduction partitioning ( $v_{SP,L}/v_{S,L}$ ) ranges from subducting-plate-motion-controlled ( $v_{SP,L}/v_{S,L} > 0.5$ , such as for Sunda and Mexico–Central America) to trench-motion-controlled ( $v_{SP,L}/v_{S,L} < 0.5$ , such as for Scotia and Cascadia).

Previous research suggests that plate age correlates with subducting plate velocity (9, 10) and trench velocity (11), but early work on global trench velocities contradicts the latter correlation (12). Other research suggests that plate velocity

is controlled by plate boundary fraction that is a subduction margin (13), but this provides no explanation for the global variation in trench velocity.

We present results from a global compilation of present-day subduction zone kinematics for 17 subduction zones and three-dimensional numerical models of buoyancy-driven progressive free subduction of a dense four-layer plate into a stratified linear-viscous mantle (14). In the models, the plate has a strong viscous core 300 times more viscous than the upper mantle; however, because it is only 25 km thick, the lithosphere is still weak with respect to bending (15–17), in accordance with slab geometries, slab pull forces, and geoid signatures at subduction zones (5, 15, 17, 18). The subducting plate is laterally homogeneous, and slab width ( $W$ )—the trench-parallel extent of a subducted slab that is limited by its lateral slab edges—varies between 300 and 7000 km. The causes for lateral slab edge formation are manifold, including slab tearing, slab window (gap) formation, subduction termination, and slab detachment.

The global data set of current subduction kinematics indicates negligible to moderate correlations between plate boundary fraction that is a subduction margin and  $v_{SP,L}$  (Fig. 1A) and between plate age and  $v_{SP,L}$  or  $v_{TL}$  (Fig. 1, B and C). In contrast, both the global data set and the dynamic models show that average  $v_{SP,L}$ ,  $v_{TL}$ , and  $v_{SP,L}/v_{S,L}$  vary nonlinearly with  $W$  along with strong correlations (Fig. 2). In nature and models,  $v_{SP,L}/v_{S,L}$  and  $v_{SP,L}$  show a nonlinear increase with increasing  $W$ , whereas  $v_{TL}$  shows a nonlinear decrease.

The nonlinear increase of  $v_{SP,L}$  with  $W$  (Fig. 2, A and D) can be explained with Stokes-like sinking of an oblate ellipsoid (analog for slab) parallel

<sup>1</sup>School of Geosciences, Monash University, Melbourne, Victoria 3800, Australia. <sup>2</sup>Scripps Institution of Oceanography, University of California, San Diego, La Jolla, CA 92093, USA.

<sup>3</sup>School of Earth Sciences, University of Melbourne, Melbourne, Victoria 3010, Australia. <sup>4</sup>School of Mathematical Sciences, Monash University, Melbourne, Victoria 3800, Australia. <sup>5</sup>Bureau of Meteorology, Melbourne, Victoria 3001, Australia.

\*To whom correspondence should be addressed. E-mail: wouter.schellart@monash.edu

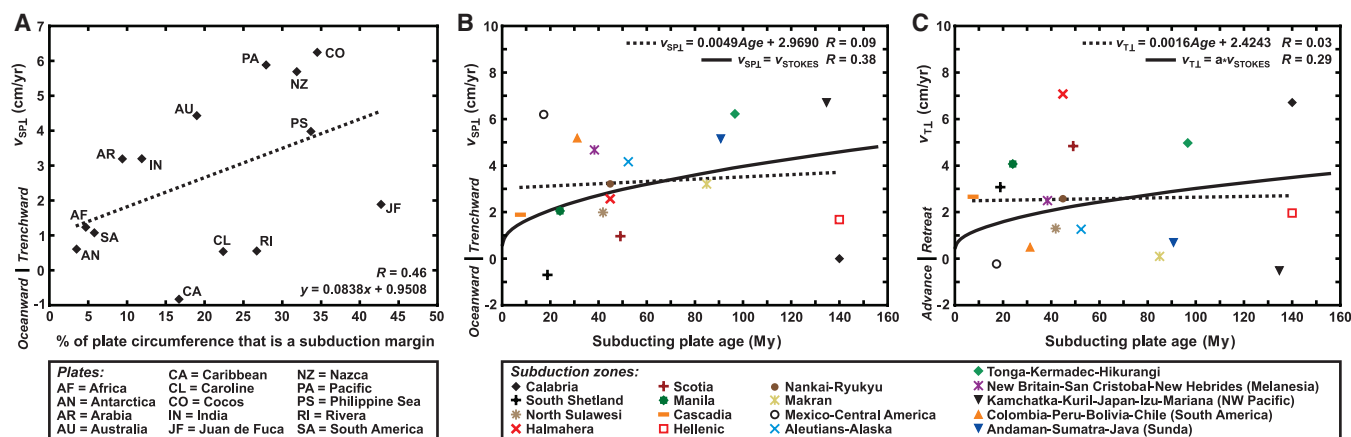


**Fig. 1.** Low to moderate correlations of subduction kinematics as a function of two subduction zone parameters (14). (A) Average trench-normal subducting plate velocity ( $v_{SP,\perp}$ ) for 14 plates as a function of percentage of plate circumference connected to a slab. (B) Average  $v_{SP,\perp}$  as a function of average subducting plate age at the trench for 17 subduction zones. (C) Average trench-normal trench migration velocity ( $v_{TL}$ ) as a function of average subducting plate age at the trench for 17 subduction zones. Uncertainty in average age is

$\pm 20\%$  for Makran,  $\pm 30\%$  for Calabria and Hellenic, and not more than  $\pm 10\%$  for others (14). Dotted lines indicate linear best-fit lines. Continuous lines in (B) and (C) indicate best-fit nonlinear curves for  $v_{SP,\perp}$  and  $v_{TL}$  assuming slab age-dependent Stokes sinking for upper mantle slabs (10, 14). Correlation in (A) is statistically not significant at 95% confidence level, and correlations for the nonlinear curves in (B) and (C) are statistically not significant at 90% confidence level using Fisher's  $z$ .

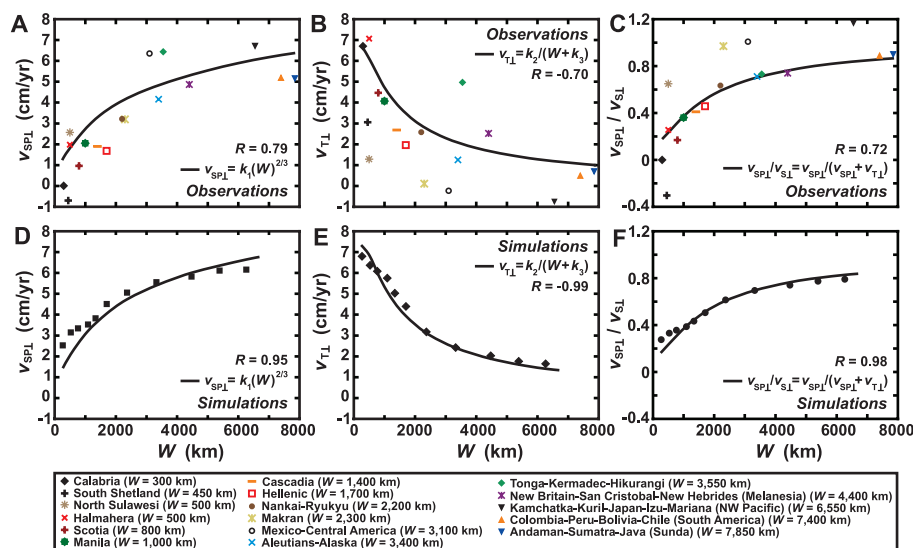


**Fig. 2.** Diagrams showing the influence of slab width ( $W$ ) on (A and D) the trench-normal subducting plate velocity ( $v_{SP,\perp}$ ), (B and E) the trench-normal trench migration velocity ( $v_{TL}$ ), and (C and F) the subduction partitioning ratio ( $v_{SP,\perp}/v_{SL}$ ). Data in (A) to (C) are from observations of 17 subduction zones on Earth, and data in (D) to (F) are from 11 numerical models of progressive subduction (14). Plots of the numerical models include time-weighted mean  $v_{SP,\perp}$ ,  $v_{TL}$ ,  $v_{SP,\perp}/v_{SL}$ , and  $W$ . We excluded subduction zones for which the average  $v_{SL} \leq 1.5$  cm/year. Correlations in (A) to (C) are statistically significant at 99% confidence level, and correlations in (D) to (F) are statistically significant at 99.9% confidence level using Fisher's  $z$ .

to its flat side by using an analytical formulation:  $v_{SP,\perp} = k_1(W)^{2/3}$ , with  $k_1 = S\Delta\rho g(LT)^{2/3}/18c_1\eta_{UM}$  (14). Here,  $S$  is the shape factor (19);  $\Delta\rho$  is the density contrast between ellipsoid and fluid;  $g$  is the gravitational acceleration;  $L$  and  $T$  are the ellipsoid length and thickness, respectively;  $c_1$  is a constant; and  $\eta_{UM}$  is the upper mantle viscosity. The nonlinear decrease of  $v_{TL}$  with  $W$  (Fig. 2, B and E) is explicable in terms of mantle return flow required for lateral slab migration, which is quasi-toroidal and occurs exclusively around the lateral slab edges (5, 7, 8, 20). The viscous resistance to such flow originates from

viscous drag at the slab-mantle interface, scaling with the slab surface area (and thus with  $W$ ), and from viscous drag at the upper-lower mantle boundary, scaling with  $W^2$  (14). Therefore, the velocity is approximately inversely dependent on  $W$ :  $v_{TL} \approx k_2/(W + k_3)$ , where  $k_2 = 2c_2\Delta\rho gLTz_{UM}/\pi\eta_{UM}$ ,  $k_3 = (4L/\pi)(1 + T/W)$ ,  $c_2$  is a constant, and  $z_{UM}$  is the upper mantle thickness (14). Because  $v_{SP,\perp}/v_{SL} = v_{SP,\perp}/(v_{SP,\perp} + v_{TL})$ , the nonlinear increase of  $v_{SP,\perp}/v_{SL}$  with  $W$  (Fig. 2, C and F) is also explained.

The control of  $W$  on  $v_{SP,\perp}/v_{SL}$  (Fig. 2) affects many aspects of Earth dynamics, including upper plate deformation, slab geometry, potential slab

ponding at the transition zone, style of mantle flow, mantle anisotropy, and chemical heterogeneity in the mantle. This relation explains the rapid motion and high partitioning of the Pacific, Nazca, Australian, and Cocos plates ( $v_{SP,\perp} \geq 4$  cm/year and  $v_{SP,\perp}/v_{SL} > 0.70$ ) (Fig. 2, A and C) by the wide slabs attached to these plates (3100 to 7850 km). Slab age cannot explain such fast motion because average subducting plate velocities for Nazca and Pacific are similar (5.7 and 5.9 cm/year, respectively), whereas average ages at the trench are appreciably different [33 and 105 million years (My), respectively] (Fig. 1).

The Juan de Fuca plate has the largest percentage of subduction zone plate boundary of all plates (43%), yet it is one of the slowest subducting plates (average  $v_{SP,\perp} = 1.9$  cm/year) (Fig. 1A). We suggest that slow motion and low partitioning of the Juan de Fuca plate (mean  $v_{SP,\perp}/v_{SL} = 0.41$ ) result predominantly from its narrow slab ( $\sim 1400$  km), enhancing slab rollback driven by its own negative buoyancy. Such rollback is consistent with the complex upper mantle anisotropy observed beneath the western United States (3) and active Basin and Range extension directed toward the Cascadia subduction zone (21).

The Juan de Fuca plate is currently one of the smallest plates on Earth, but in the geological past (referred to as Farallon plate) it was much larger. Indeed, the Farallon plate and slab decreased dramatically in trench-parallel extent by an order of magnitude during Cenozoic eastward subduction below the west coast of the Americas (Fig. 3A), resulting in a decrease in  $v_{SP,\perp}/v_{SL}$  and  $v_{SP,\perp}$  (Fig. 3B). Applying the best-fit curves for  $v_{SP,\perp}/v_{SL}$  and  $v_{SP,\perp}$  from the numerical models (Fig. 2, D and F) to the Farallon plate, we can explain the decrease in  $v_{SP,\perp}/v_{SL}$  from 0.8 to 0.4 and most ( $\sim 70\%$ , or  $\sim 5$  cm/year) of the decrease in  $v_{SP,\perp}$  from  $\sim 9$  to  $\sim 2$  cm/year (Fig. 3B). The moderate decrease in slab age from  $\sim 35$  to  $\sim 10$  My during the Cenozoic

(Fig. 3C) might account for another  $\sim 1$  cm/year ( $\sim 15\%$ ) of decrease in  $v_{SP,L}$ , as suggested by the best-fit nonlinear curve for slab age and  $v_{SP,L}$  (Fig. 1B). Furthermore, the fraction of Farallon plate boundary that existed as a subduction zone cannot explain any decrease in  $v_{SP,L}$  because it increased slightly during the Cenozoic (Fig. 3C).

The progressive decrease in Farallon slab width can also explain the temporal and spatial change in overriding plate deformation in North America [shortening during the Sevier-Laramide orogeny in the Cretaceous to Early Eocene (22), followed by widespread extension from the Eocene to present in the Basin and Range province (23)]. These episodes of contrasting deformation took place during continued trench retreat and west-to-southwestward motion of the North American plate (24) (Fig. 3, B and D to H). During the Late Cretaceous and Early Cenozoic, the subducting Farallon slab was very wide ( $>10,000$  km), resisting slab retreat, but was pushed back by the overriding North American plate (Fig. 3D), which was rapidly driven westward because of fast poloidal corner flow and strong basal tractions resulting from rapid Farallon plate motion. This caused major overriding plate shortening in North America, in places exceeding 300 km (22), and would have

enhanced flat slab subduction of the Farallon plate. As the slab segmented and slab windows started to form, slab width decreased and quasi-toroidal return flow around the lateral slab edges increased, which initiated slab-buoyancy-driven trench retreat, caused upper-plate extension (Fig. 3, E to H), and facilitated slab steepening. Furthermore, slower Farallon plate velocities reduced poloidal corner flow rates and basal tractions below North America. This might explain the Cenozoic slowing of the North American plate (Fig. 3, B and D to H) and the general decrease in spreading velocities in the northern Atlantic Ocean (25).

The gravitational potential energy stored in the thickened orogenic crust facilitated Basin and Range extension (26) and migration of the subduction hinge. Furthermore, in conjunction with the weakened (hot) lithosphere due to the overriding plate setting and the protracted period of orogenesis [ $\sim 100$  My (22)], this energy storage promoted the distributed style of deformation in the Basin and Range, as predicted by geodynamic models of lithospheric extension (27). Because extension occurred over a vast area (Fig. 3, F to H), we argue that it is not a consequence of asthenosphere upwelling above the Californian slab window as previously proposed (28); the hor-

izontally projected extent of the window was at least an order of magnitude smaller than the extent of Basin and Range extension at 30 to 20 million years ago (Ma).

Buoyancy-driven slab retreat and incipient extension started in the Eocene at the northern edge of the Farallon slab ( $\sim 45$  Ma) when a slab window formed at the Pacific-Farallon-North American triple junction because of different subduction velocities on either side of the junction (Fig. 3E). This window grew dramatically when subduction stopped north of the triple junction and a northern slab edge formed, further enhancing rollback and causing widespread extension in the northern Basin and Range (Fig. 3F). Another slab window formed in the Baja California region at  $\sim 30$  Ma (29) with slab edges on each side, allowing efficient mantle return flow and slab rollback that subsequently lead to widespread extension in the southern Basin and Range (Fig. 3F). The proposed slab behavior is in accordance with the model results, which show that wide slabs ( $\sim 4000$  to  $7000$  km) retreat near their lateral edges because of efficient toroidal-type mantle return flow (fig. S3C) (20). At  $\sim 15$  Ma, slab width reduced to only  $\sim 2300$  km (Fig. 3A), allowing buoyancy-driven rollback for the whole slab, as observed in

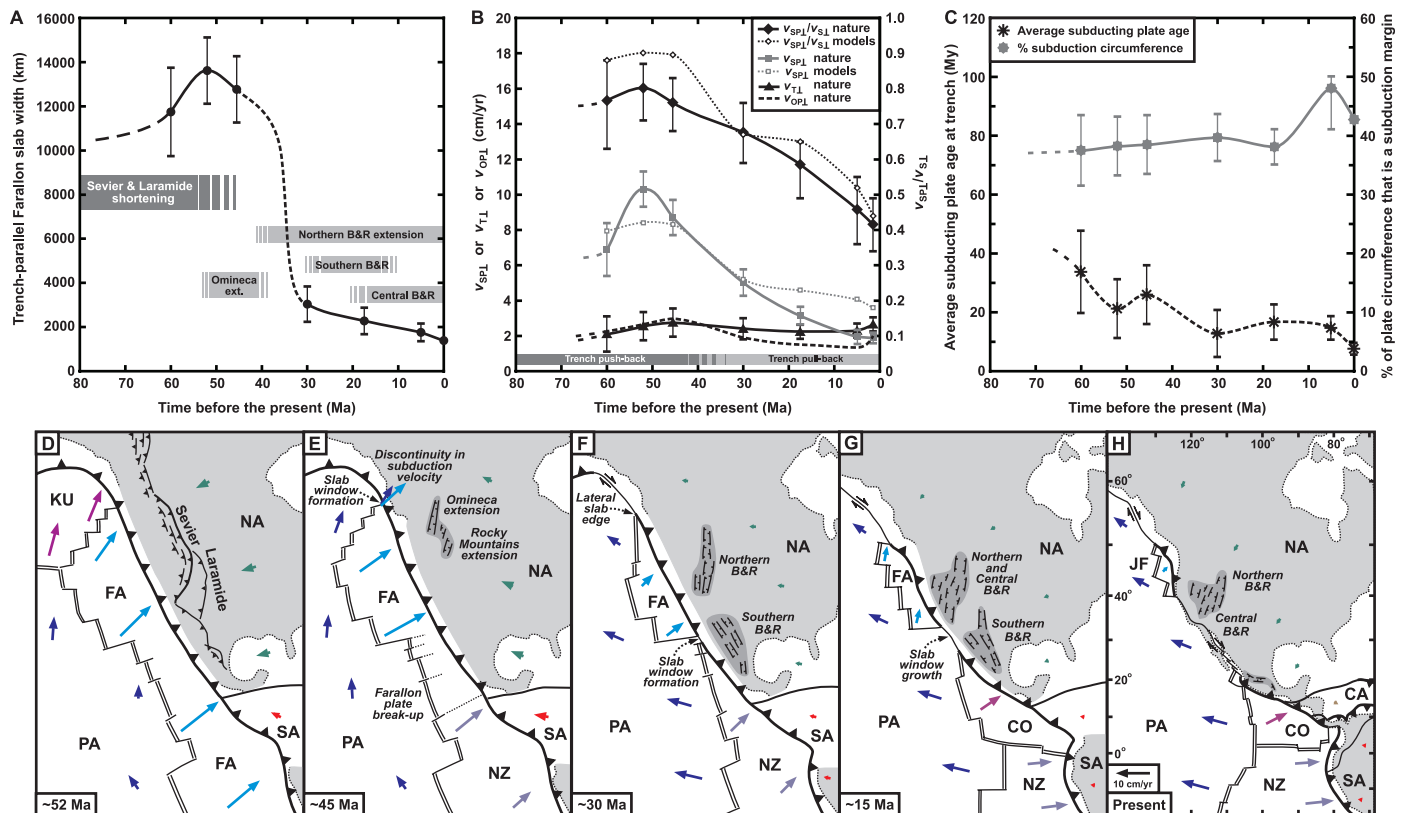


**Fig. 3.** The kinematics and several physical characteristics of the Farallon plate during the Cenozoic (14). (A) Evolution of trench-parallel Farallon slab width ( $W$ ) [compiled from (24, 29)]. (B) Evolution of average subduction partitioning ( $v_{SP,L}/v_{S,L}$ ), trench-normal subducting plate velocity ( $v_{SP,L}$ ), trench-normal trench velocity ( $v_{T,L}$ ), and trench-normal overriding plate velocity ( $v_{OP,L}$ ) with data compiled from (22–24). Also shown is timing of trench push-back ( $v_{T,L} < v_{OP,L}$ ) and trench pull-back ( $v_{T,L} > v_{OP,L}$ ). (C) Evolution of percentage of Farallon plate circumference that is connected

to a slab and evolution of average Farallon slab age at the trench (14). (D to H) Reconstructions of the Farallon-western North American subduction margin at (D)  $\sim 52$  Ma (Early Eocene), (E)  $\sim 45$  Ma (Middle Eocene), (F)  $\sim 30$  Ma (Oligocene), (G)  $\sim 15$  Ma (Middle Miocene), and (H) 0 Ma (present). Reconstructions were compiled from (22–24, 29), and plate motions are from (24). Plate abbreviations are CA, Caribbean; CO, Cocos; FA, Farallon; JF, Juan de Fuca; KU, Kula; NA, North America; NZ, Nazca; PA, Pacific; SA, South America.



models with narrow and intermediate-width slabs (fig. S3, A and B). Such rollback drove the main phase of Basin and Range extension (Fig. 3, G and H).

### References and Notes

1. R. M. Russo, P. G. Silver, *Science* **263**, 1105 (1994).
2. M. D. Long, P. G. Silver, *Science* **319**, 315 (2008).
3. G. Zandt, E. Humphreys, *Geology* **36**, 295 (2008).
4. E. Di Giuseppe, J. van Hunen, F. Funicello, C. Faccenna, D. Giardini, *Geochim. Geophys. Geosyst.* **9**, Q02014 (2008).
5. W. P. Schellart, *Geochim. Geophys. Geosyst.* **9**, Q03014 (2008).
6. C. Kincaid, R. W. Griffiths, *Nature* **425**, 58 (2003).
7. W. P. Schellart, *J. Geophys. Res.* **109** (B7), B07401 (2004).
8. D. R. Stegman, J. Freeman, W. P. Schellart, L. Moresi, D. May, *Geochim. Geophys. Geosyst.* **7**, Q03012 (2006).
9. R. L. Carlson, T. W. C. Hilde, S. Uyeda, *Geophys. Res. Lett.* **10**, 297 (1983).
10. S. Goes, F. A. Capitanio, G. Morra, *Nature* **451**, 981 (2008).
11. P. Molnar, T. Atwater, *Earth Planet. Sci. Lett.* **41**, 330 (1978).
12. R. D. Jarrard, *Rev. Geophys.* **24**, 217 (1986).
13. D. W. Forsyth, S. Uyeda, *Geophys. J. R. Astron. Soc.* **43**, 163 (1975).
14. Materials and methods are available as supporting material on *Science* Online.
15. F. A. Capitanio, G. Morra, S. Goes, *Geochim. Geophys. Geosyst.* **10**, Q04002 (2009).
16. G. Morra, K. Regenauer-Lieb, D. Giardini, *Geology* **34**, 877 (2006).
17. D. R. Stegman, R. Farrington, F. A. Capitanio, W. P. Schellart, *Tectonophysics* **483**, 29 (2010).
18. L. Moresi, M. Gurnis, *Earth Planet. Sci. Lett.* **138**, 15 (1996).
19. R. C. Kerr, J. R. Lister, *J. Geol.* **99**, 457 (1991).
20. W. P. Schellart, J. Freeman, D. R. Stegman, L. Moresi, D. May, *Nature* **446**, 308 (2007).
21. C. Kreemer, W. C. Hammond, *Geology* **35**, 943 (2007).
22. P. G. DeCelles, *Am. J. Sci.* **304**, 105 (2004).
23. L. J. Sonder, C. H. Jones, *Annu. Rev. Earth Planet. Sci.* **27**, 417 (1999).
24. R. G. Gordon, D. M. Jurdy, *J. Geophys. Res.* **91** (B12), 12389 (1986).
25. R. D. Müller, M. Sdrolias, C. Gaina, W. R. Roest, *Geochim. Geophys. Geosyst.* **9**, Q04006 (2008).
26. L. M. Flesch, W. E. Holt, A. J. Haines, B. Shen-Tu, *Science* **287**, 834 (2000).
27. W. R. Buck, *J. Geophys. Res.* **96** (B12), 20161 (1991).
28. W. R. Dickinson, W. S. Snyder, *J. Geol.* **87**, 609 (1979).
29. T. Atwater, *Geol. Soc. Am. Bull.* **81**, 3513 (1970).
30. We appreciate discussions and interactions with R. Kerr, R. Govers, F. Capitanio, S. Zlotnik, M. Sandiford, R. Griffiths, and R. Weinberg. We thank the Victorian Partnership for Advanced Computing, the National Computational Infrastructure, and AuScope for computational resources and technical support. This work was supported by an award under the Merit Allocation Scheme on the National Computational Infrastructure National Facility at the Australian National University. W.P.S. was supported by a QE II Fellowship and Discovery grant DP0771823 from the Australian Research Council, a Monash Fellowship from Monash University, and a J. G. Russell Award from the Australian Academy of Science. D.R.S. was supported in part by a Centenary Research Fellowship from the University of Melbourne and in part by the G. Unger Vetlesen Foundation. L.M. and R.J.F. were supported by Discovery grant DP0878501.

### Supporting Online Material

[www.sciencemag.org/cgi/content/full/329/5989/316/DC1](http://www.sciencemag.org/cgi/content/full/329/5989/316/DC1)  
Materials and Methods

Figs. S1 to S3

Table S1

References

1 April 2010; accepted 11 June 2010

10.1126/science.1190366

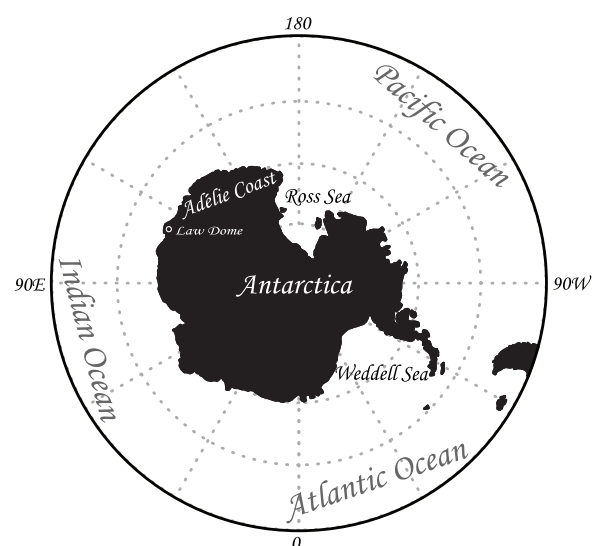
# Simulated Rapid Warming of Abyssal North Pacific Waters

Shuhei Masuda,<sup>1\*</sup> Toshiyuki Awaji,<sup>2,3</sup> Nozomi Sugiura,<sup>2</sup> John Philip Matthews,<sup>3,4</sup> Takahiro Toyoda,<sup>1</sup> Yoshimi Kawai,<sup>1</sup> Toshimasa Doi,<sup>1</sup> Shinya Kouketsu,<sup>1</sup> Hiromichi Igarashi,<sup>2</sup> Katsuro Katsumata,<sup>1</sup> Hiroshi Uchida,<sup>1</sup> Takeshi Kawano,<sup>1</sup> Masao Fukasawa<sup>1</sup>

Recent observational surveys have shown significant oceanic bottom-water warming. However, the mechanisms causing such warming remain poorly understood, and their time scales are uncertain. Here, we report computer simulations that reveal a fast teleconnection between changes in the surface air-sea heat flux off the Adélie Coast of Antarctica and the bottom-water warming in the North Pacific. In contrast to conventional estimates of a multicentennial time scale, this link is established over only four decades through the action of internal waves. Changes in the heat content of the deep ocean are thus far more sensitive to the air-sea thermal interchanges than previously considered. Our findings require a reassessment of the role of the Southern Ocean in determining the impact of atmospheric warming on deep oceanic waters.

The densest waters of the world's oceans are formed around Antarctica where heat exchange with the atmosphere and subsequent ice formation create uniquely dense water masses that sink rapidly and move northward. This Antarctic Bottom Water (AABW) (1, 2) remains largely isolated from further heat exchange as it spreads over much of the world's ocean floor. By replenishing the supply of AABW, highly productive source regions such as the Weddell and Ross seas (Fig. 1) play an important

**Fig. 1.** Antarctic region. The Weddell and Ross seas are major source regions for Antarctic Bottom Water because here the dense, cold, and relatively saline shelf waters formed through air-sea heat exchange sink down the continental slope into the deep Southern Ocean.



<sup>1</sup>Research Institute for Global Change, Japan Agency for Marine-Earth Science and Technology (JAMSTEC), Yokohama 236-0001, Japan. <sup>2</sup>Data Management and Engineering Department, Data Research Center for Marine-Earth Sciences, JAMSTEC, Yokohama 236-0001, Japan. <sup>3</sup>Department of Geophysics, Kyoto University, Kyoto 606-8502, Japan. <sup>4</sup>Environmental Satellite Applications, Llys Awel, Mount Street, Menai Bridge LL595BW, UK.

\*To whom correspondence should be addressed. E-mail: smasuda@jamstec.go.jp